

Thermal effects on the performance of ultrasonically welded CF/PPS joints and its correlation to the degree of crystallinity at the weldline

Koutras, N.; Benedictus, R.; Villegas, I. Fernandez

DOI

[10.1016/j.jcomc.2020.100093](https://doi.org/10.1016/j.jcomc.2020.100093)

Publication date

2021

Document Version

Final published version

Published in

Composites Part C: Open Access

Citation (APA)

Koutras, N., Benedictus, R., & Villegas, I. F. (2021). Thermal effects on the performance of ultrasonically welded CF/PPS joints and its correlation to the degree of crystallinity at the weldline. *Composites Part C: Open Access*, 4, Article 100093. <https://doi.org/10.1016/j.jcomc.2020.100093>

Important note

To cite this publication, please use the final published version (if applicable). Please check the document version above.

Copyright

Other than for strictly personal use, it is not permitted to download, forward or distribute the text or part of it, without the consent of the author(s) and/or copyright holder(s), unless the work is under an open content license such as Creative Commons.

Takedown policy

Please contact us and provide details if you believe this document breaches copyrights. We will remove access to the work immediately and investigate your claim.



Thermal effects on the performance of ultrasonically welded CF/PPS joints and its correlation to the degree of crystallinity at the weldline

N. Koutras*, R. Benedictus, I. Fernandez Villegas

Aerospace Structures and Materials Department, Faculty of Aerospace Engineering, Delft University of Technology, Kluyverweg 1, 2629 HS Delft, the Netherlands

ARTICLE INFO

Keywords:

Ultrasonic welding
Thermoplastic composites
Thermal analysis
Temperature
Failure mechanism
Crystallinity

ABSTRACT

The effect of temperature on the lap shear strength (LSS) and failure mechanisms of ultrasonically welded carbon fibre reinforced polyphenylene sulphide (CF/PPS) joints was investigated, correlating the weld performance to the crystallinity degree of PPS at the weldline. The single-lap shear tests were carried out at temperatures ranging from $-50\text{ }^{\circ}\text{C}$ to $120\text{ }^{\circ}\text{C}$ on three series, one with amorphous and two with semi-crystalline weldline. The overall trend was decreasing LSS with increasing temperature and the largest LSS reduction was observed above the glass transition temperature. Fractographic analysis revealed that the main failure mechanism at $-50\text{ }^{\circ}\text{C}$ was matrix fracture while fibre/matrix debonding became more pronounced with increasing temperature. It was demonstrated that higher degree of crystallinity of PPS at the weldline was beneficial at high temperatures ($90\text{ }^{\circ}\text{C}$ and $120\text{ }^{\circ}\text{C}$) most likely due to the higher fibre/matrix interfacial strength compared to amorphous PPS. The amorphous weldline was shown to be advantageous at $-50\text{ }^{\circ}\text{C}$, probably due to the higher toughness and ductility of amorphous PPS.

1. Introduction

To date, the effect of temperature on the mechanical performance of thermoplastic composites (TPC) welded joints has not been studied extensively. The work presented in [1] demonstrated that the strength of resistance welded glass fibre reinforced polyphenylene sulphide (GF/PPS) joints was governed by the strength of fibre/matrix interface at all temperatures. In addition, it was also suggested that the increase in testing temperature may partially relieve the compressive radial stresses, formed between the fibres and the matrix during cooling, and weaken the mechanical interlocking of the matrix around the fibres. Rohart et al [2] found that resistance welded CF/PPS joints exposed to a wide range of temperatures above room temperature (RT) primarily failed at the interface between the heating element and the matrix. In both studies, the largest reduction in lap shear strength (LSS) occurred at temperatures higher than the glass transition temperature (T_g) of PPS.

To the authors' knowledge, no studies on the effect of temperature on ultrasonically welded (UW) TPC joints have been published. Thus far, much research on ultrasonic welding of thermoplastic composites has been published focusing on the fundamental phenomena of the process [3–6], on the optimisation of the process [7–11], and on the development and optimisation of continuous ultrasonic welding [12,13]. Fracture of UW TPC joints at RT conditions primarily occurs within the composite

substrates as broken fibres bundles can be seen on the fracture surfaces [7,8]. It is well known that increasing temperature can cause strength and modulus reductions in polymers [14,15], having also a detrimental effect on the fibre/matrix interfacial strength [16–19]. Considering the effect of temperature on the elastic modulus of the matrix and the fibre/matrix interfacial strength, as well as the effect of temperature on resistance welded TPC joints, it seems plausible to expect that temperature could have a detrimental effect on UW TPC joints as well.

Apart from the temperature-dependent properties of TPC, another important factor that can influence the performance of UW TPC joints is the physical state of the polymer at the weldline. In a previous study [20], it was shown that the ultrasonic welding process parameters had a profound effect on the matrix crystallinity; depending on the welding force and the vibration amplitude, the PPS matrix at the weldline of UW CF/PPS joints could be predominantly amorphous or semi-crystalline. The changes in crystallinity can have a significant effect on properties such as the elastic modulus, the fibre/matrix interfacial strength, the fracture toughness and the glass transition temperature. Gao and Kim showed that increasing cooling rates had a negative effect on the interfacial shear strength of carbon fibre reinforced polyetheretherketone (CF/PEEK) composites [21,22]. Likewise, annealing of CF/PPS led to enhanced fibre/matrix interfacial shear strength [23,24]. On the contrary, a lower crystallinity degree was found to result in higher Mode-I interlaminar fracture toughness for CF/PEEK and CF/PPS laminates, as

* Corresponding author.

E-mail address: n.koutras@tudelft.nl (N. Koutras).

Table 1
Preparation conditions of single-lap joints.

Specimen series	Welding force (N)	Vibration amplitude (μm)	Optimum travel (mm)	Thermal treatment (post welding)
ASW_F	1000	86.2	0.15	-
ASW_S	300	51.8	0.13	-
ANN_F	1000	86.2	0.15	2 h, 200 °C

reported by several researchers [21,25,26]. Furthermore, lower crystallinity degree has been found to cause a reduction in the T_g of the matrix by several degrees Celsius [27–29]. Hence, in view of the effect of the ultrasonic welding process parameters on the matrix crystallinity at the weldline of UW joints, it is of interest to investigate the weld performance with respect to the crystallinity degree of the matrix weldline.

Considering the very few studies on thermal effects on TPC welded joints, in conjunction with the use of high performance thermoplastics in demanding applications, operating in a wide range of temperatures, it becomes clear that the exposure of UW TPC joints to low and high temperatures is of significant importance. With this background in mind, this paper investigates the effect of temperature on the lap shear strength and the failure mechanisms of ultrasonically welded CF/PPS joints by linking the weld performance to the degree of crystallinity of PPS at the weldline. This paper also provides a clear view of the advantages and disadvantages of amorphous and semi-crystalline weldlines of ultrasonically welded CF/PPS joints, with respect to the weld performance at different service temperatures. A thorough experimental research plan consisting of three series of ultrasonically welded CF/PPS single-lap joints, of varying crystallinity degrees at the weldline, was carried out at a wide range of temperatures measuring the lap shear strength of the joints, accompanied by micrographic analysis of the fracture surfaces.

2. Experimental procedure

2.1. Materials & laminate manufacturing

The material used in this study was Cetex® woven (five harness satin) CF/PPS supplied by Ten Cate Advanced Composites, The Netherlands. $[(0^\circ/90^\circ)_3]_3$ laminates were produced using a hot platen press at 320 °C and 1 MPa pressure for 20 min and subsequently cooled down at a cooling rate of 15 °C/min. The details of the manufacturing method can be found in [20]. 0° is the direction of the warp yarns and 90° is the direction of the weft yarns of the woven fabric. The consolidated laminates had a final measured thickness of 1.9 mm, with a nominal 50% fibre volume content. The welding adherends, measuring 101 mm in length and 25.4 mm in width, were cut from the consolidated laminates using a water-cooled diamond blade. The main apparent fibre orientation on the outer surfaces of the adherends was parallel to the longitudinal direction. Flat energy director (ED) films were also prepared using the hot platen press at 270 °C and 1 MPa pressure for 20 min. The ED films are made of the same polymer as the adherends' matrix and are placed between the adherends prior to welding in order to concentrate the heat generation during ultrasonic welding [7–9]. The ED films were cooled down at 15 °C/min and their final measured thickness was 0.24 mm.

3. Ultrasonic welding

All the joints in this study were welded in a single-lap configuration using a 20 kHz Rinco 3000 microprocessor-controlled ultrasonic welder with maximum power output of 3000 W (Rinco Ultrasonics, Romanshorn, Switzerland). The overlap area of the joints was 25.4 mm long and 12.7 mm wide. The ultrasonic welding process was displacement-controlled and the optimum travel values are summarised in Table 1. Further information on the ultrasonic welding process followed in this work can be found in [20] where the process has been described in more detail.

Table 2

Number of single-lap joint specimens tested at each temperature.

Specimen Series	# of specimens					
	-50 °C	20 °C	50 °C	70 °C	90 °C	120 °C
ASW_F	5	5	5	6	14	10
ASW_S	7	6	6	6	7	6
ANN_F	9	5	8	10	10	8

As mentioned in the introduction section, three series of single-lap joints of varying crystallinity degrees at the weldline were prepared under different conditions. One series was prepared using a set of high welding force and high vibration amplitude, (1000 N, 86.2 μm), representing the fast welding process, and one using a set of low welding force and low vibration amplitude, (300 N, 51.8 μm), representing the slow welding process. According to the results shown in [20], the former yielded predominantly amorphous PPS at the weldline (2.4%) while the latter yielded a weldline of moderate PPS crystallinity (14.6%). A third series was prepared by annealing the welded joints, which were obtained using the fast welding process, for 2 hours at 200 °C inside an oven. It should be noted that the specimens were “free-standing” in the oven (i.e. no applied pressure) during the annealing process. The welding and annealing conditions for the three series of joints used in this study are summarised in Table 1. Regarding the nomenclature of the specimen series, ASW stands for as-welded, ANN stands for annealed, F stands for fast welding process and S stands for slow welding process.

3.1. Characterisation of Welded Joints

3.1.1. Lap Shear Tests

Single-lap shear (SLS) tests based on the ASTM D1002 standard [30] were performed at different temperatures within the -50 °C to 120 °C range. A 250kN Zwick/Roell universal testing machine operating at 1.3 mm/min cross-head speed and a temperature chamber were used for the tests. Prior to each test, the temperature chamber was pre-heated for 1 h at the test temperature. All specimens were maintained at each test temperature for 10 min prior to the tests in order to reach thermal equilibrium. The tests at -50 °C were performed using liquid nitrogen to reach cryogenic temperatures. The apparent LSS of the welded joints was calculated as the maximum load divided by the average overlap area (25.4 mm \times 12.7 mm). A minimum of 5 specimens were tested per joint type and testing temperature. The total number of specimens tested at each temperature are summarised in Table 2.

3.1.2. Fractography

Fractographic analysis was conducted through a stereo microscope (Zeiss stereo Discovery V8) and a scanning electron microscope (SEM) from JEOL (JSM-7500F) in order to investigate the failure mechanisms of the welded joints. The macroscopic images of the fracture surfaces were captured using the stereo microscope, while the detailed images at high magnification were captured using the SEM. Prior to the SEM analysis, the fracture surfaces were sputter coated with a thin layer of gold to prevent charging. It is important to note that the stereo-microscope images are of limited relevance in the fractographic analysis presented in Section 3.2.2. The purpose of the stereo-microscope images is to assist the analysis by providing the view of the entire fracture surfaces,

Table 3
Preparation conditions of DSC specimens.

Series ID	Welding conditions		Post-welding conditions	LSS series correspondence
	Welding force (N)	Vibration amplitude (μm)	Thermal treatment	
ED_Ref ¹	n/a	n/a	-	n.a.
ED_F ¹	1000	86.2	-	ASW_F
ED_S ¹	300	51.8	-	ASW_S
ANN_Ref	n/a	n/a	2 h, 200 °C	ANN_F
CON_F	1000	86.2	10 min, 120 °C	ASW_F at 120 °C
CON_S	300	51.8	10 min, 120 °C	ASW_S at 120 °C

¹ Specimens measured and presented in [20].

illustrating macroscopic features such as voids and resin rich areas and showing the exact locations where the SEM images were captured.

3.2. Thermal analysis

Differential Scanning Calorimetry (DSC) was used in order to determine the degree of crystallinity of PPS specimens prepared under different conditions in order to complement the work presented in [20]. All DSC specimens were heated from 25 °C to 310 °C at 10 °C/min, in a Sapphire DSC from Perkin Elmer. The degree of crystallinity, X_C , was determined from the heating run and was computed using the following equation:

$$X_C = \frac{\Delta H_m - \Delta H_c}{\Delta H_f^o} * 100 (\%) \quad (1)$$

Where ΔH_m is the measured specific melting enthalpy in J/g, ΔH_c is the specific energy associated with the cold crystallization peak in J/g, and ΔH_f^o is the specific melting enthalpy of an ideal crystal ($\Delta H_f^o = 112 \text{ J/g}$) [31]. The melting peak temperature and the specific melting enthalpy were calibrated prior to the experiments by using Indium standard.

Table 3 presents the DSC series investigated in this study. The first three series of Table 3 were tested and presented in a previous study [20], while the other three series were prepared and tested during this study. Four series were ED films removed from the weldline, from which, two were subjected to thermal treatment after welding. Two series were ED films prior to welding, one as the reference material and one as the annealed material. The preparation conditions (when applicable) are presented in Table 3, in which the correspondence of each DSC series to the LSS series is also shown.

Since the Tg of PPS is below 120°C [1], both CON_F and CON_S were prepared in order to examine the influence of conditioning – prior to the SLS tests – for 10 min at 120 °C on the crystallinity degree of PPS. The abbreviation CON stands for “conditioned”. It must be noted that due to the lack of ANN_Ref samples at the time of DSC tests, the annealing effect was studied on fully amorphous PPS films (same PPS films used to produce the ED). Considering the very low X_C of ASW_F (2.4% as reported in [20]), it was expected that annealing at 200 °C for 2 h should yield similar levels of X_C . Nonetheless, the main objective of this study was to compare specimens of crystallinity levels that differ significantly and not by just below 5%. The ED films were easily removed from the weldline due to the use of Kapton films between each adherend and the ED: prior to ultrasonic welding, two 25 μm thick Kapton films were fixed with an adhesive tape to each adherend and the ED was sandwiched between them. The method to remove the ED films after welding has been described in detail in [20].

Dynamic Mechanical Analysis (DMA) was carried out using a Pyris Diamond DMA from Perkin Elmer to determine the glass transition temperature and the evolution of the storage and loss moduli of neat PPS films with temperature. One amorphous PPS film and one annealed PPS film were tested in tension. All tests were performed within the temperature range of -50 °C to 200 °C, at a frequency of 1 Hz and a heating rate of 2 °C/min. The dimensions of the neat PPS films were 20 mm \times 10 mm \times 0.08 mm.

Thermomechanical Analysis (TMA) was used to measure the coefficient of thermal expansion (CTE) of neat PPS films. The TMA specimens were cut in 15 mm \times 3 mm \times 0.08 mm films and the experiments were performed at a heating rate of 2 °C/min in a Diamond TMA from Perkin Elmer. Similarly to the DMA tests, the films tested were amorphous PPS, within the -50 °C to 150 °C range and annealed PPS (2 h at 200 °C), within the 20 °C to 140 °C range. The TMA measurements on amorphous PPS films have already been presented in [1]. Liquid nitrogen was used in both DMA and TMA tests in order to reach the cryogenic temperatures, however, at the moment of performing the TMA tests on annealed PPS it was not possible to reach cryogenic temperatures due to technical issues. It must be noted that it was not possible to test the removed ED films on TMA and DMA since the films were physically distorted from the welding process (i.e. showing creases and being slightly buckled), which could have influenced the accuracy of the DMA and TMA measurements. Therefore, it was decided to proceed with testing only amorphous and annealed PPS films, as the two extreme cases of crystallinity degree. The behaviour of ASW_F was considered to be closer to the one of amorphous PPS, due to the low crystallinity degree of the former, and the behaviour of ASW_S somewhere in between amorphous PPS and annealed PPS due to its moderate value of crystallinity degree.

4. Results

4.1. Thermal analysis

Fig. 1 illustrates the degree of crystallinity as obtained from the DSC measurements on the PPS films listed in Table 3. It can be seen that ANN_Ref had a similar X_C (23.4%) to ED_Ref (26%) while ED_S showed a moderate X_C (14.6%) and ED_F was predominantly amorphous exhibiting a X_C of 2.4%. Annealing for 10 min at 120 °C brought about a significant increase in the crystallinity of the removed ED films, as demonstrated by CON_F and CON_S, which both exhibited a X_C of 21.3%. In addition, annealing for 10 min at 120 °C also resulted in lower scatter. An important point to be made, though, is that CON_F showed larger scatter than CON_S. This could potentially mean that, during annealing, the crystallization of PPS across the ED_F film was not as uniform as the one across the ED_S film. Considering the small size of DSC samples (less than 10 mg), and that not all areas of CON_F had the same crystallinity degree amongst them, it is possible to have a larger scatter in the measurements. The non-uniform crystallization was most likely the reason for the large scatter in ED_S measurements as well. As it was presented in [20], the appearance of ED_S films was opaque with some transparent areas, indicating that not all areas across ED_S were of equal crystallinity.

The DMA measurements on amorphous and annealed PPS are shown in Fig. 2, where the storage modulus (E') and loss modulus (E'') curves of both specimens are presented. Obtained from the E'' peak, the Tg of ANN_Ref was found to be higher than the Tg of amorphous PPS, 108 °C and 91 °C, respectively. The difference in the glass transition temperature is also demonstrated in the E' curves, as the drop in E' corresponding to the Tg, occurred below 90 °C in amorphous PPS and close to 100 °C

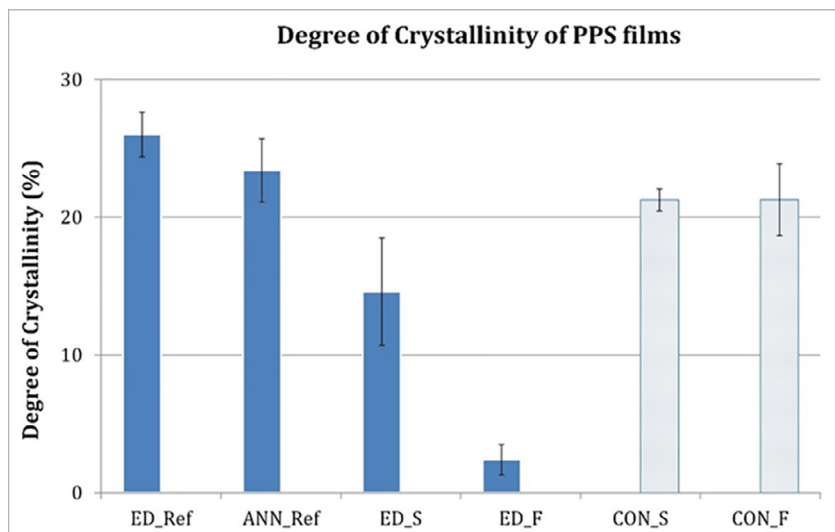


Fig. 1. Crystallinity degree of PPS films calculated from DSC measurements.

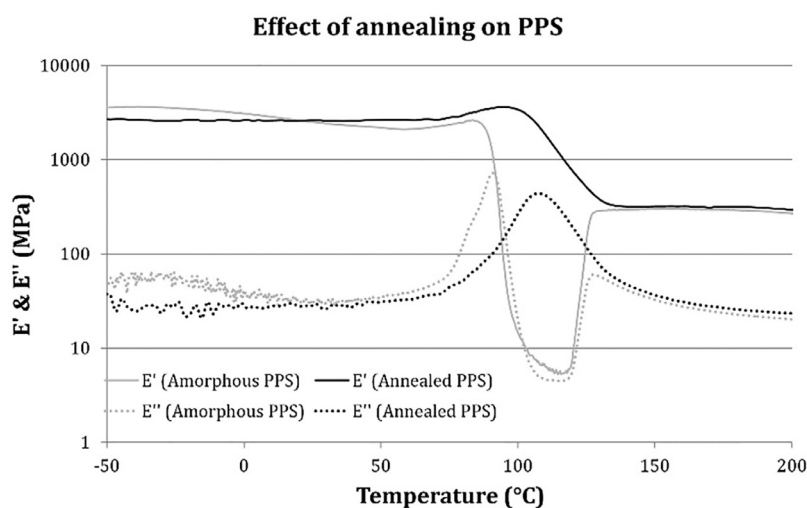


Fig. 2. Dynamic mechanical analysis of amorphous PPS and annealed PPS.

in annealed PPS. Furthermore, the E' of amorphous PPS started to increase around 120 °C, an increase that continued until 130 °C, where E' reached a plateau. On the contrary, the E' of annealed PPS continuously decreased until it reached a plateau around 130 °C. The increase in E' of amorphous PPS could be attributed to the cold crystallization of PPS which occurs around 120 °C, as shown in previous studies [20,32]. The mobility of the molecular chains increases at temperatures above the T_g , and around 120 °C the molecular chains have obtained enough mobility which allows them to rearrange into crystals. Another feature of Fig. 2 is the slight increase in E' of both films, just before the drop in E' that corresponds to the T_g . This increase is not so common but has been observed before [33,34]. Barnes and Byerly [33] considered it as a test artefact, having a negligible effect on their results. Menard [34] attributed the phenomenon to molecular rearrangement causing stress relief at the glass transition temperature. This phenomenon, either being simply a test artefact or molecular rearrangement, did not interfere with the interpretation of the DMA results, having a negligible effect on them. Furthermore, it is worthwhile to comment on the abrupt decrease of the storage modulus of amorphous PPS. While the drop in E' signifies the glass transition, the reduction was much higher than expected. This of course can be attributed partially to the high chain mobility of amorphous PPS in the absence of crystalline domains, however, it can also be attributed to the presence of frozen stresses which

were relieved as the polymer entered its glass transition region. The DMA measurements were carried out on as-received amorphous PPS films without any prior thermal treatment after film processing. During quenching (processing) of the films, thermal stresses developed and remained in the films (as residual stresses). Thus, upon heating during the DMA tests, those stresses were relieved, causing molecular rearrangement and possibly contributing to this large drop in E' .

The thermal expansion of amorphous and annealed PPS measured through TMA are illustrated in Fig. 3. The amorphous PPS expanded significantly above 83 °C, while the annealed PPS exhibited an increase in its expansion rate at a higher temperature (above 92 °C), an increase that was much smaller than the one of amorphous PPS. It is important to mention, though, that this much larger increase in the thermal expansion of the amorphous PPS film compared to the thermal expansion of the annealed PPS film could have its origin not only in the enhanced chain mobility of amorphous polymers due to the absence of crystalline domains, but also in the presence of frozen stresses that were relieved close to the T_g . Similarly to the DMA measurements, the TMA measurements were carried out on as-received amorphous PPS films without prior thermal treatment after film processing. Hence, similarly to the abrupt drop in E' of amorphous PPS in Fig. 2, it could be possible that the large thermal expansion was caused by molecular rearrangement as well. Two additional points to be noted from this graph are the lo-

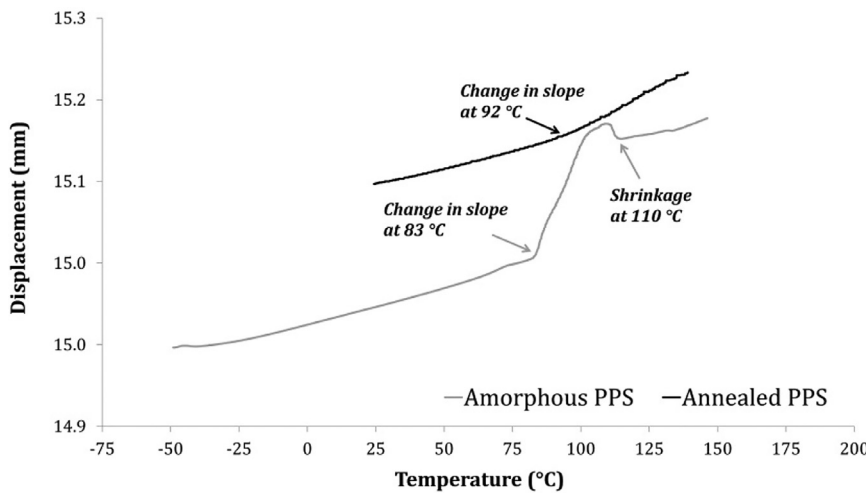


Fig. 3. Thermal expansion of amorphous PPS (a) and annealed PPS (b) obtained through TMA tests. The glass transition is indicated by the change in slope which is caused by the increase of the expansion rate.

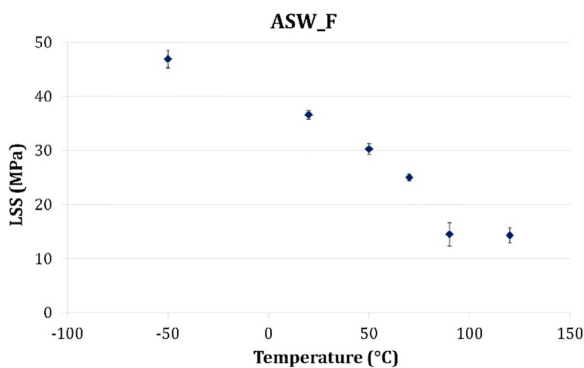


Fig. 4. Temperature dependence of lap shear strength of ASW_F.

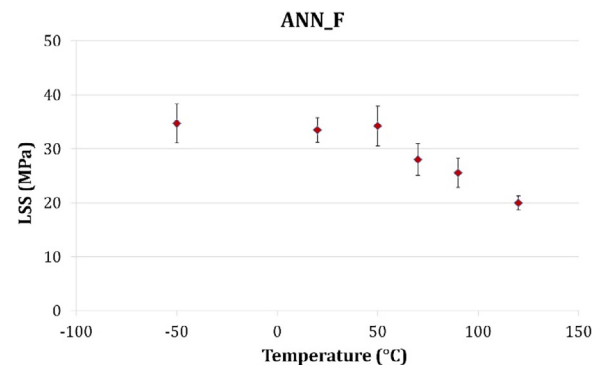


Fig. 6. Temperature dependence of lap shear strength of ANN_F.

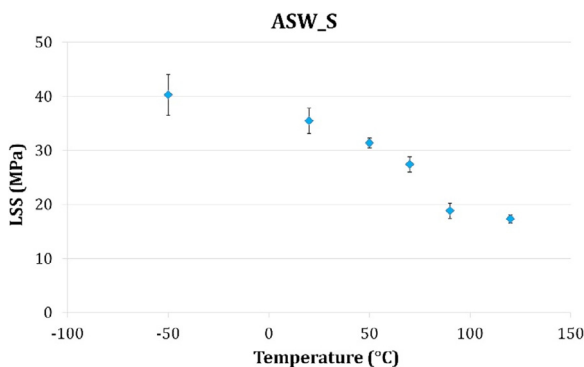


Fig. 5. Temperature dependence of lap shear strength of ASW_S.

cal maximum at 110 °C in the amorphous specimen, a behaviour that was not observed in the annealed specimen and could be attributed to shrinkage caused by cold crystallization, and the significant decrease in thermal expansion rate following this local maximum.

4.2. Single-lap shear tests

4.2.1. Lap shear strength

Figs. 4 and 5 illustrate the temperature dependence of the LSS of ASW_F and ASW_S, respectively. The highest LSS was obtained at -50 °C

for both series (28% and 14% higher than at RT for ASW_F and ASW_S, respectively). Both series exhibited a linear decrease between RT and 70 °C, with ASW_S having a smaller slope compared to ASW_F, indicating a lower decrease in LSS of ASW_S within this temperature range. However, at 90 °C the reduction in LSS was significant for both series, not following the initial linear trend: about 60% and 47% reduction compared to RT for ASW_F and ASW_S, respectively. Further increase in temperature did not lead to further strength reduction for ASW_F and only resulted in a minor decrease for ASW_S. Another notable feature in Fig. 4 is the relatively high scatter of the LSS of ASW_F at 90 °C (coefficient of variation, CoV, of 15%, as opposed to below 10% and 4% at 120 °C and at the other testing temperatures, respectively). In the case of ASW_S, the scatter was below 10% at all testing temperatures, with the highest CoV amounting to 9% at -50 °C.

Fig. 6 illustrates the temperature dependence of LSS of ANN_F. The behaviour of the annealed series differs notably from the behaviour of both as-welded series. The LSS of the annealed series between -50 °C and 50 °C remained almost constant, while the reduction at 90 °C with respect to RT (equal to 24%) was not as high as in the other two series. Furthermore, increasing the temperature to 120 °C caused a LSS reduction of 22% with respect to 90 °C, as opposed to the minor or negligible reduction found in the other two series (Figs. 4 and 5). Moreover, the scatter of the annealed series was high at most temperatures (i.e. CoV higher than 10%) except at RT and 120 °C (CoV lower than 7%). The origin of the larger scatter of ANN_F is briefly discussed in Section 4, also in light of the fractographic analysis presented in Section 3.2.2.

Table 4

Summary of SLS test results on UW CF/PPS joints showing the average LSS together with the standard deviation at each temperature.

Specimen series	Lap shear strength (MPa)					
	-50 °C	RT	50 °C	70 °C	90 °C	120 °C
ASW_F	46.9 ± 1.6	36.6 ± 0.8	30.3 ± 1.0	25.0 ± 0.7	14.5 ± 2.2	14.3 ± 1.4
ASW_S	40.3 ± 3.8	35.5 ± 2.4	31.4 ± 0.9	27.4 ± 1.4	18.8 ± 1.4	17.3 ± 0.7
ANN_F	34.7 ± 3.6	33.5 ± 2.3	34.2 ± 3.7	28.0 ± 3.0	25.6 ± 2.7	20.0 ± 1.3

The comparison of the LSS at each temperature amongst the three series (Table 4), shows that at -50 °C and at RT, ASW_F exhibited the highest LSS followed by ASW_S. At 50 °C and above, the ANN_F specimens exhibited the highest LSS amongst the three series, while the ASW_F exhibited the lowest.

4.2.2. Fractography

In the present section, the results from the fractographic inspection are presented. First, a summary of the most important fractographic features and failure mechanisms at all testing temperatures is provided, followed by a detailed fractographic analysis on representative fracture surfaces at -50 °C and 120 °C for each series. The fracture surfaces at -50 °C and at 120 °C represent the extreme cases of this study, thus, the more representative ones. From the inspection of the fracture surfaces at temperatures equal or higher than RT, it was observed that the primary failure mechanisms of ASW_F and ASW_S specimens was fibre/matrix debonding, which became more prominent with increasing temperature. Furthermore, the failure locus was always in the 1st ply. Fibre/matrix debonding occurred at -50 °C as well, however, to a much lesser degree since most of the carbon fibres had residual matrix on their surfaces, suggesting matrix fracture as the main failure mechanism. Regarding the failure location, both 1st ply and 2nd ply failure were observed at -50 °C. Increasing temperature also rendered the matrix more ductile, as the occurrence of ductile matrix failure increased, especially at 90 °C and 120 °C, where limited brittle failure could be observed. The analysis of the fracture surfaces of ANN_F specimens revealed that cohesive failure (i.e. failure within the resin rich area of the weldline) and 1st ply failure occurred in all specimens at all temperatures. Cohesive failure was the dominant failure mechanism at -50 °C but its occurrence diminished with increasing temperature, whereas fibre/matrix debonding became more pronounced. Similarly to the other two series, matrix ductility was also more pronounced with increasing temperature. Furthermore, a significant amount of voids was observed in all cases of ANN_F specimens regardless the testing temperature. It is suggested that the formation of voids was a consequence of the annealing process since the porosity levels in the ANN_F joints was much higher than the porosity in the ASW_F joints, which was limited to the overlap edges. This is suggested because both series were welded using the same welding process parameters, however, only ANN_F exhibited high porosity. Only at 120 °C, ASW_F specimens exhibited similar porosity levels to ANN_F specimens. This was probably due to the 10 min pre-conditioning at 120 °C of the ASW_F joints prior to testing, which, in fact, supports the idea that the voids were a product of the annealing process. It follows a detailed analysis of representative fracture surfaces of specimens tested at -50 °C and 120 °C, the two extreme testing temperatures in this study.

4.2.2.1. Fracture surfaces at -50 °C. Figs. 7 and 8 illustrate, respectively, the fracture surfaces of one ASW_F specimen and one ASW_S specimen, both tested at -50 °C. The 2nd ply failure can be seen in almost half of the fracture surfaces of both specimens (enclosed in the dashed squares). A secondary feature of the fracture surface of ASW_S (Fig. 8) is the presence of voids in some areas at the overlap edges.

With the assistance of SEM, closer looks of the fracture surfaces in Figs. 7 and Fig. 8 were captured and shown in Fig. 9 and Fig. 10,

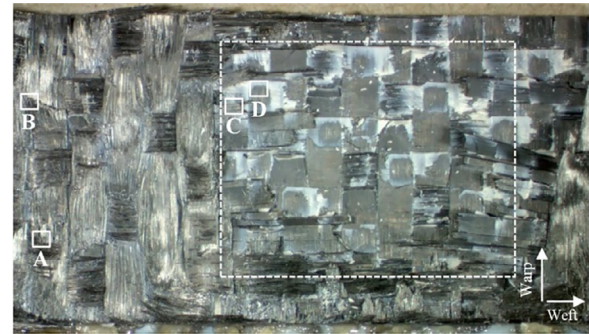


Fig. 7. Fracture surface of an ASW_F specimen tested at -50 °C showing 1st ply failure and 2nd ply failure (the 2nd ply failure is enclosed within the dashed square). A–D represent the locations at which the SEM micrographs were captured.

respectively. Both fracture surfaces exhibited very similar fractographic features, mainly matrix fracture and occasionally fibre/matrix debonding. The SEM micrographs revealed exposed carbon fibres, which indicated the occurrence of fibre/matrix debonding, however, in most areas the carbon fibres had matrix remnants on their surfaces (Fig. 9A, Fig. 10A and Fig. 10B). In Fig. 9B, extensive fibre/matrix debonding can also be observed, however, the features in Fig. 9B were less dominant throughout the entire fracture surface than the features in Fig. 9A. Furthermore, both ductile and brittle matrix failure modes were identified. Matrix ductility was signified by deformed matrix which was drawn over the carbon fibres surfaces, a fractographic feature that was observed in several locations and illustrated here in Figs. 9B and 10B. In the work of D. Purslow on matrix fractography of fibre-reinforced thermoplastics [35], large amount of plastic deformation and matrix drawing prior to failure were identified as characteristics of a ductile failure. In Fig. 9B, the matrix has been drawn, resulting in bare fibres surrounded by plastically deformed matrix (“elongated” features). Another manifestation of matrix ductility can be seen in Fig. 9C where deformed matrix was smeared across the fracture surface. Brittle matrix failure appeared to occur more frequently than ductile matrix failure, especially in ASW_F specimens. Brittle failure was identified by characteristic features like cusps (Fig. 10A) while plastic deformation was limited (Figs. 9D, 10C and 10D). It is interesting to note that brittle failure features were mainly found in areas where failure occurred in the 2nd ply.

Fig. 11 illustrates the fracture surface of an ANN_F specimen tested at -50 °C where both 1st ply failure and cohesive failure at the weldline occurred. The fracture surface appears to have a substantial amount of resin rich areas, and the occurrence of cohesive failure was confirmed by the SEM micrographs (Fig. 12). An important point to be made from is the significant amount of voids that are present in the fracture surfaces of ANN_F joints.

A more detailed view of the voids is shown in Figs. 12A and 12B; the voids were randomly distributed across the entire fracture surface and their size ranged from tens to a few hundred microns. Most fibres were covered by thick resin layers (Fig. 12C), however, fibre/matrix debonding was also observed (Fig. 12D). The latter was not the most dominant

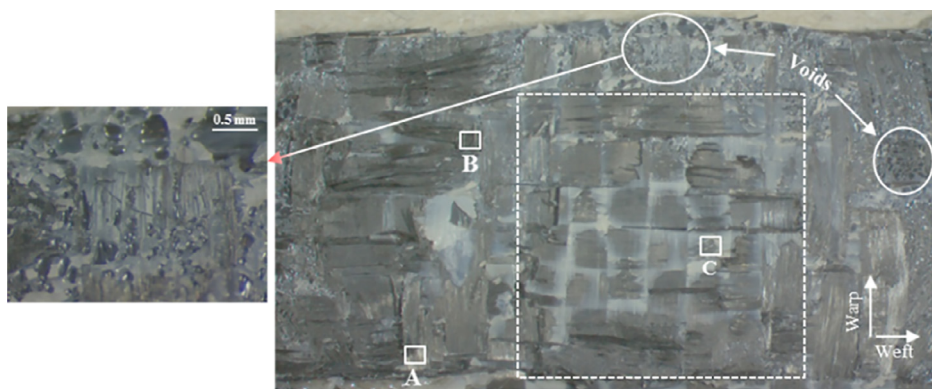


Fig. 8. Fracture surface of an ASW_S specimen tested at $-50\text{ }^{\circ}\text{C}$ showing 1st ply failure and 2nd ply failure (the 2nd ply failure is enclosed within the dashed square). In addition, voids were also observed (e.g. the two circled areas), a magnification of which is shown at the smaller left image. A, B and C represent the locations at which the SEM micrographs were captured.

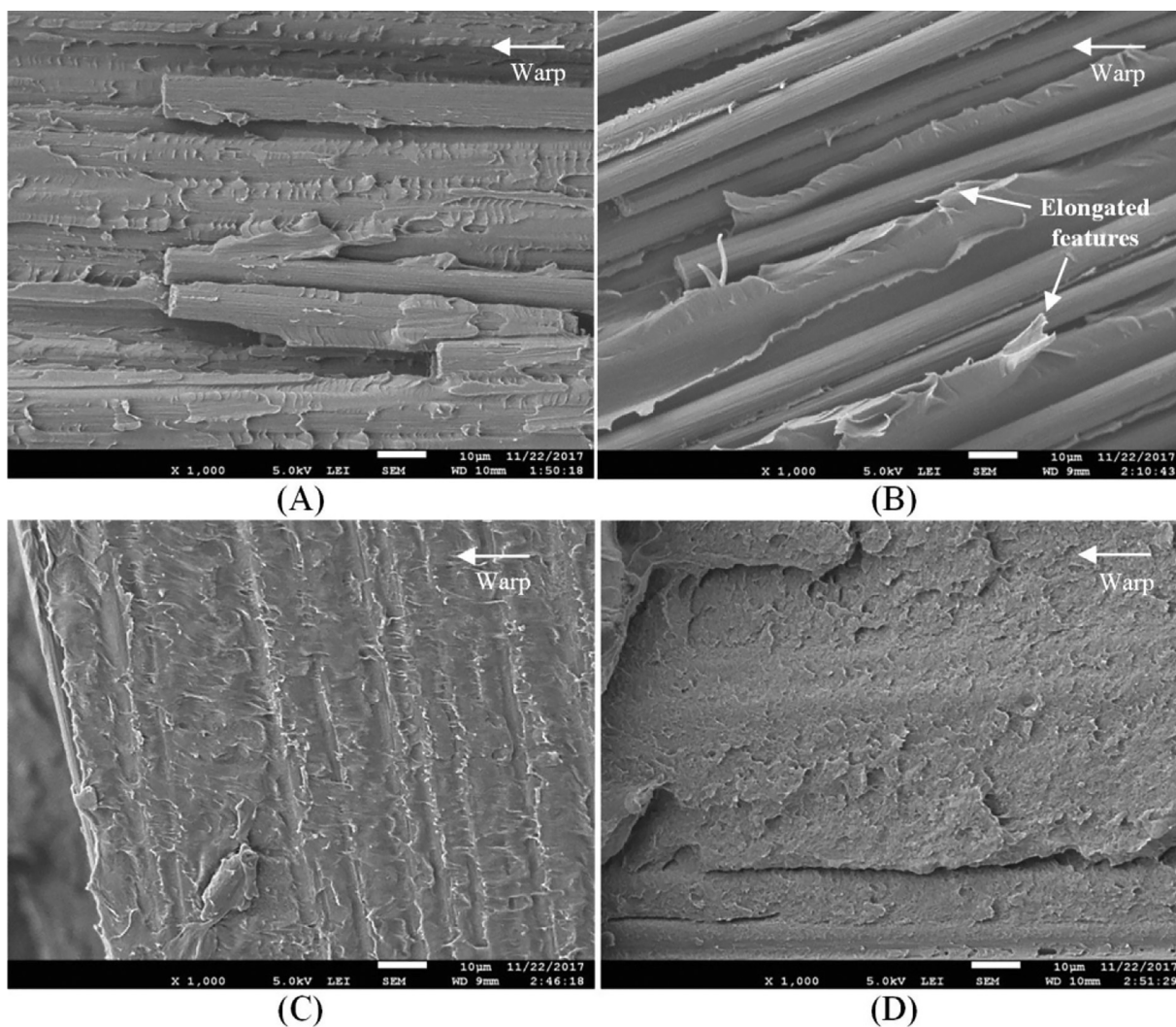


Fig. 9. SEM micrographs of locations A–D of Fig. 7: (A) Broken and exposed fibres that still have matrix remnants on their surfaces. (B) Extensive fibre/matrix debonding accompanied by considerable matrix drawing. (C) Smeared matrix indicating ductile failure. (D) Brittle failure as indicated by the limited plastic deformation. The arrow at the top right of each image indicates the warp direction.

failure mode as most of the failure occurred within the bulk matrix of the weldline (cohesive failure). Ductile matrix failure took place as the smeared matrix (Fig. 12C) and the localised matrix drawing (Fig. 12D) demonstrate, however, brittle matrix failure was more prevalent, as the overall limited plastic deformation of the matrix signified. Two exam-

ples of brittle failure can be seen in Figs. 12A and 12B, where cracks were formed within resin-rich areas of the weldline.

4.2.2.2. *Fracture surfaces at 120 °C.* Representative fracture surfaces of ASW_F and ASW_S tested at 120 °C are depicted in Fig. 13 and Fig. 14,

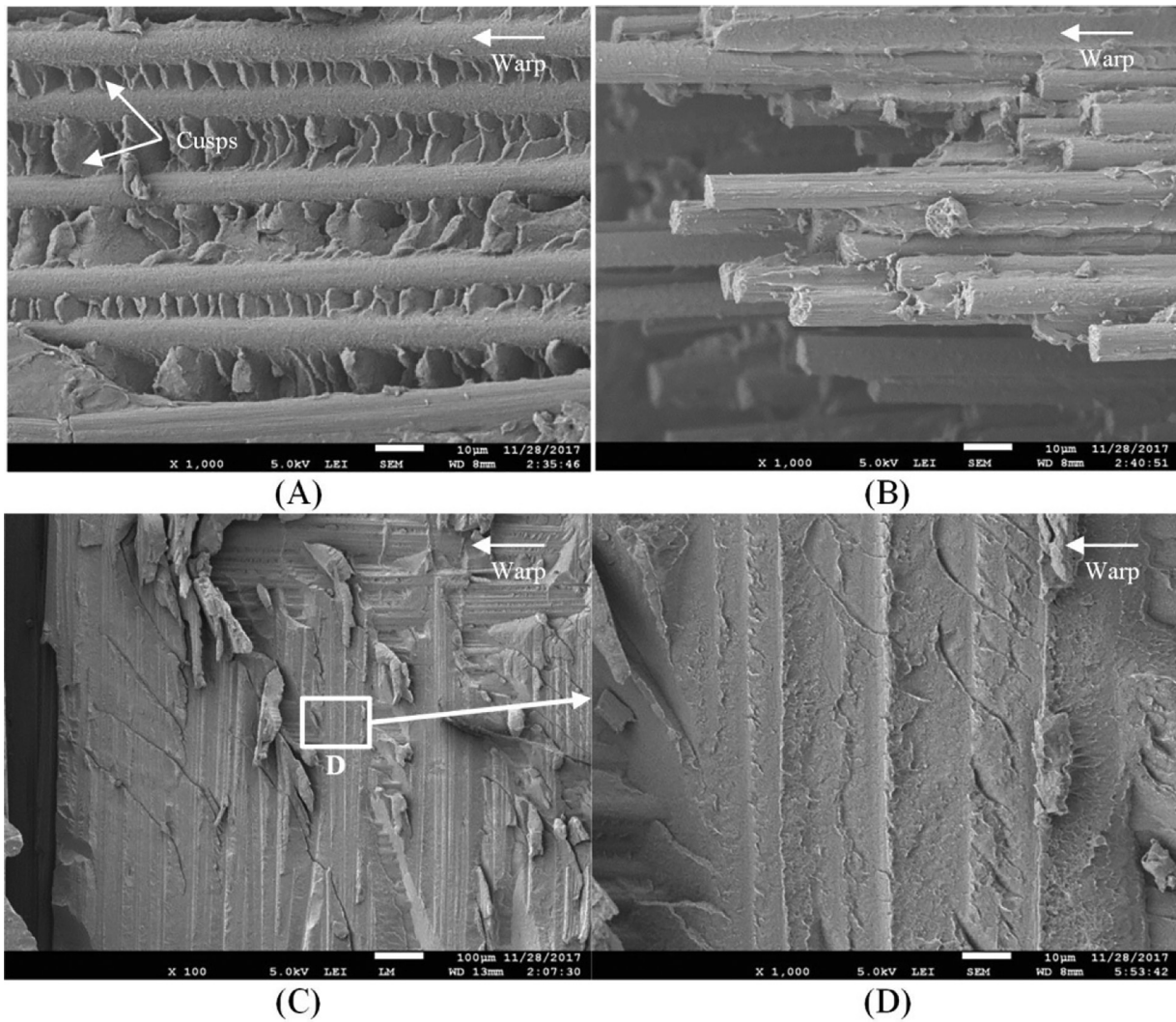


Fig. 10. SEM micrographs of locations A and B of Fig. 8: (A) Cusps, indicating brittle failure, and fibres still covered with resin. (B) Broken fibre bundle with most fibres still covered with resin. (C) Resin rich area dominated by brittle failure. (D) Magnification of location D of Fig. 10C, showing a resin rich area.

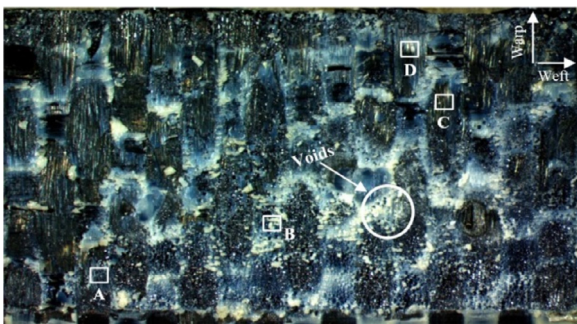


Fig. 11. Fracture surface of an ANN_F specimen tested at $-50\text{ }^{\circ}\text{C}$ showing cohesive failure accompanied by extensive areas of voids (e.g. circled area). A–D represent the locations at which the SEM micrographs were captured.

respectively. The failure occurred only in the 1st ply. In addition, the presence of voids in some areas was also observed. It is important to note that voids were present at the edges of the overlap at all temperatures,

however, at $120\text{ }^{\circ}\text{C}$ their presence was extended to other areas of the overlap and their size was similar to that of ANN_F, ranging from tens to a few hundred microns.

Closer looks at the fracture surfaces of Figs. 13 and 14 are illustrated in Fig. 15 and Fig. 16, respectively. Extensive fibre/matrix debonding, with no residual matrix left on the surfaces of the carbon fibres, appeared to be prevalent throughout the entire fracture surfaces of ASW_F and ASW_S (Fig. 15A, Fig. 15B, Fig. 16A and Fig. 16B). The occurrence of fibre/matrix debonding is demonstrated once more in Fig. 15D where the fibre imprints on the matrix can be seen. Both ASW_F and ASW_S exhibited ductile matrix failure as the substantial matrix drawing in Fig. 15B, Fig. 15D and Fig. 16B indicates. Fig. 15C shows a large amount of voids, accompanied by ductile matrix failure. The characteristic features of ductile matrix failure were seen throughout the entire fracture surface, while fractographic features associated to brittle matrix failure like cusps, as well as limited plastic deformation, were observed in limited areas.

The fracture surface of an ANN_F specimen, tested at $120\text{ }^{\circ}\text{C}$, is illustrated in Fig. 17 where 1st ply failure and cohesive failure occurred. The failure was accompanied by extensive areas of voids, similarly to

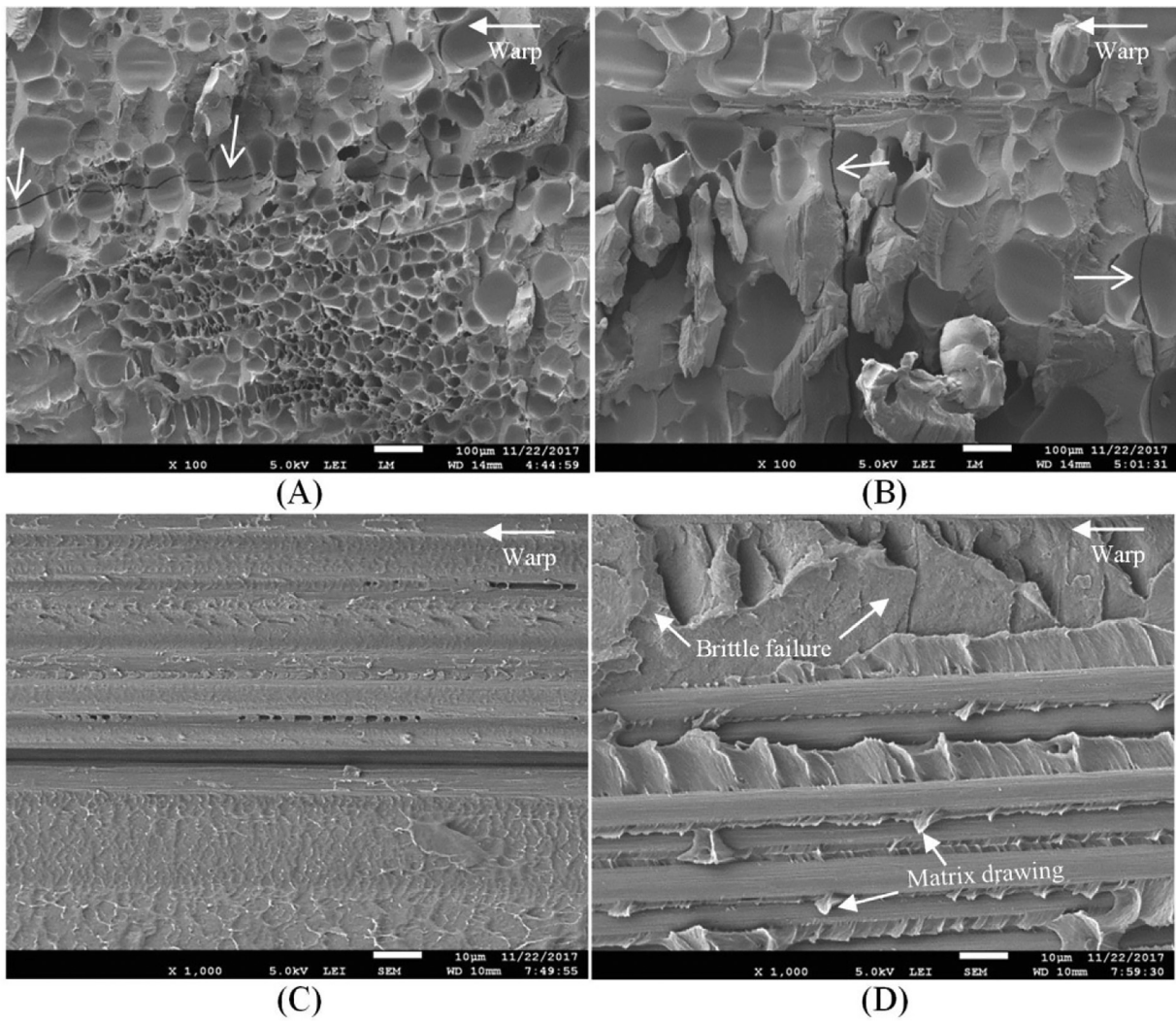


Fig. 12. SEM micrographs of locations A–D of Fig. 11: (A) & (B) Extensive areas of small and large voids, randomly distributed. Arrows point at cracks formed with limited plastic deformation. (C) Smeared matrix indicating ductile failure. (D) Combination of brittle failure, as it can be seen at the top of the picture, and ductile failure indicated by matrix drawing. Some exposed fibres can also be observed indicating fibre/matrix debonding. The arrow at the top right of each image indicates the warp direction.

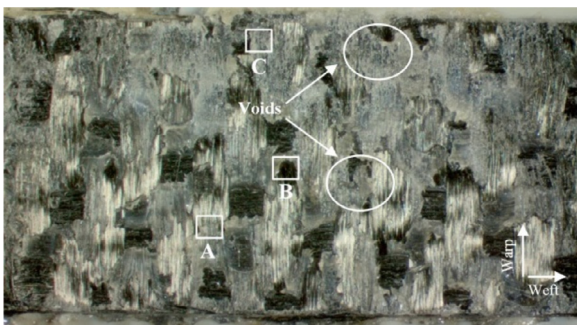


Fig. 13. Fracture surface of an ASW_F specimen tested at 120 °C showing 1st ply failure accompanied by extensive areas of voids (e.g. the two circled areas). A–C represent the locations at which the SEM micrographs were captured.

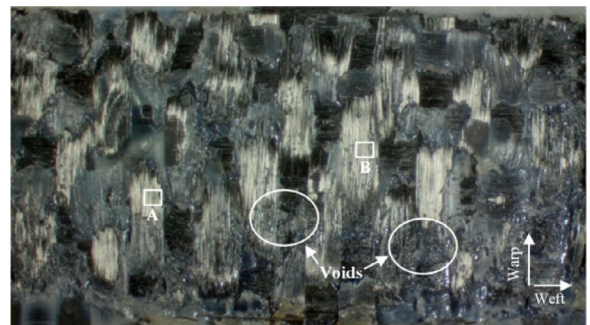


Fig. 14. Fracture surface of an ASW_S specimen tested at 120 °C showing 1st ply failure accompanied by areas of voids (e.g. the two circled areas). A and B represent the locations at which the SEM micrographs (Fig. 16) were captured.

ANN_F specimens tested at all temperatures (including -50 °C). Contrarily to ANN_F specimens tested at -50 °C, at 120 °C fibre/matrix debonding was more prevalent, as Fig. 18A and Fig. 18B demonstrate. Ductile

failure of the matrix was also prevalent at this temperature; an example of ductile failure can be seen in Fig. 18A in which a large area of matrix between the fibres is deformed.

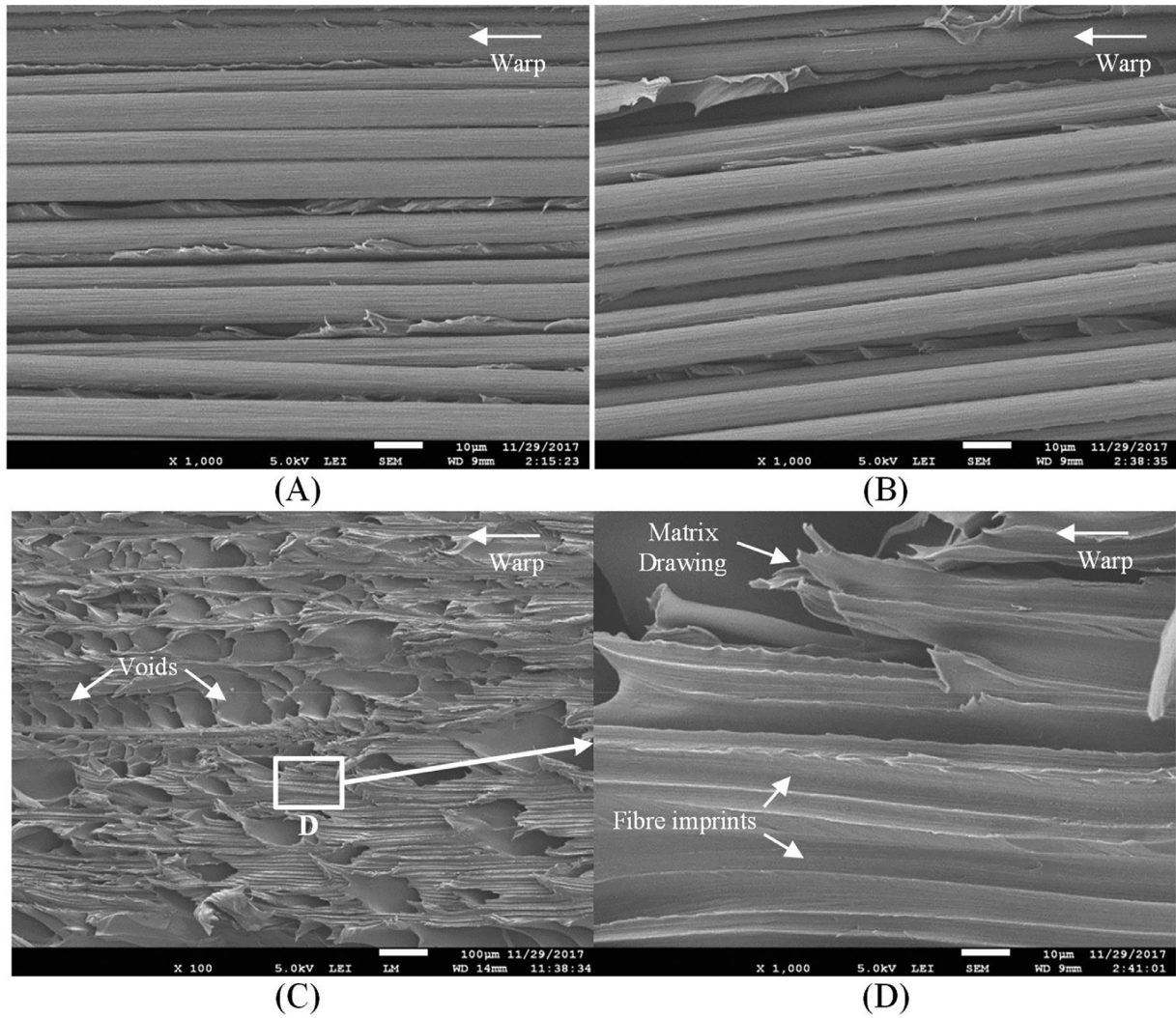


Fig. 15. SEM micrographs of locations A–C of Fig. 13: (A) & (B) Extensive fibre/matrix debonding accompanied by matrix drawing. (C) Large amount of voids accompanied by ductile failure. (D) Magnification of location D of Fig. 15C, showing substantial matrix drawing and fibre imprints.

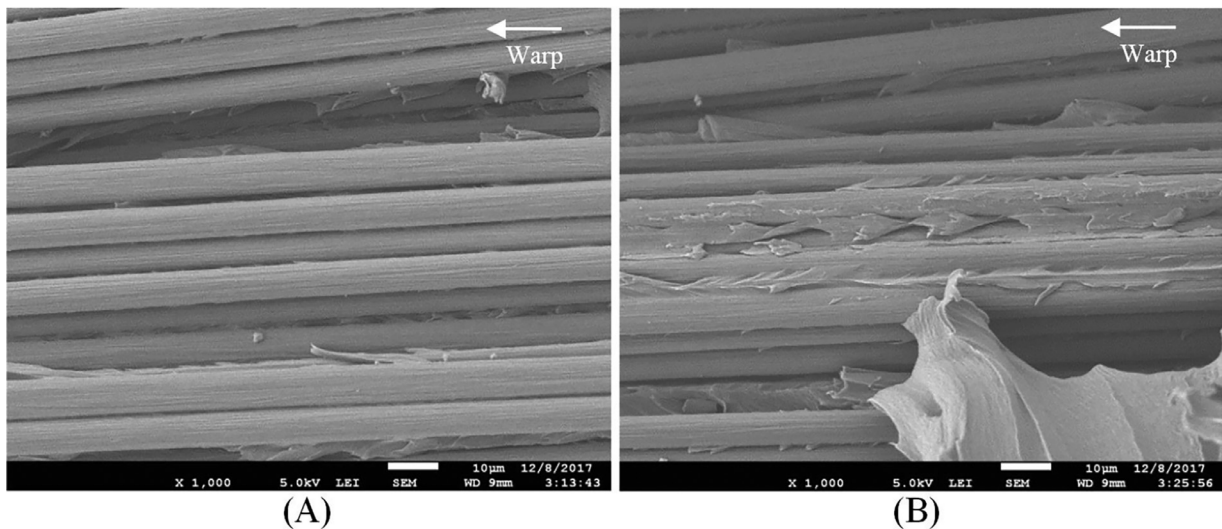


Fig. 16. SEM micrographs of locations A and B of Fig. 14: (A) & (B) Extensive fibre/matrix debonding accompanied by ductile failure.

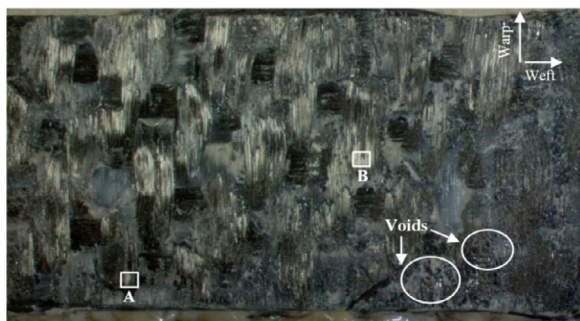


Fig. 17. Fracture surface of an ANN_F specimen tested at 120 °C showing cohesive failure accompanied by extensive areas of voids (e.g. the two circled areas). A and B represent the locations at which the SEM micrographs were captured.

5. Discussion

In this section, the influence of temperature on the LSS and the failure mechanisms of UW CF/PPS joints are discussed, followed by the correlation of the degree of crystallinity of PPS to the LSS and to the failure mechanisms.

The overall trend of the SLS tests was decreasing LSS with increasing temperature. In order to summarise the results and facilitate the reader, Fig. 19 unifies the three previous LSS graphs (Fig. 4–Fig. 6) into one chart. The main points deduced from Fig. 19 are the following:

- (i) The highest LSS was obtained at -50 °C by ASW_F.
- (ii) At -50 °C and RT, ASW_F showed higher LSS compared to the other two series, while at 50 °C and above, ANN_F exhibited higher LSS than the two as-welded series.
- (iii) At 90 °C, the LSS of ANN_F was substantially higher than the LSS of both as-welded series, namely 43% higher than ASW_F and 26% higher than ASW_S.
- (iv) The LSS of ASW_F and ASW_S remained virtually constant at 90 °C and 120 °C, while the LSS of ANN_F showed a further decrease. At 120 °C, the difference between the LSS of ANN_F and the two as-welded series decreased significantly with respect to 90 °C; the LSS of ANN_F was 28% and 13% higher than that of ASW_F and ASW_S, respectively.
- (v) At high temperatures (90 °C and 120 °C) the specimens welded with the slowest welding process (ASW_S) exhibited better me-

chanical performance than the ones with the fastest welding process (ASW_F).

The primary failure mechanism at all temperatures has been identified as fibre/matrix debonding except for -50 °C where the failure mechanism was primarily matrix fracture. The fracture morphologies of bare fibres or fibres with little amount of residual matrix on their surfaces indicate that the failure can be associated with the strength of the fibre/matrix interface. Such fractographic features were even more prevalent at higher temperatures. On these grounds, it seems fair to suggest that the LSS of UW CF/PPS joints can be related to the fibre/matrix interfacial strength and that the latter deteriorated with increasing temperature, contributing to the reduction in LSS.

As described in [1], the main mechanism governing the fibre/matrix interfacial strength in TPC is of physical (mechanical) nature which relies on the formation of compressive radial stresses around the fibres as well as on the static friction at the fibre/matrix interface. In essence, the physical bond created is the mechanical interlocking of the matrix around the fibres. As it was suggested in [1], the increase in testing temperature reduces the difference (ΔT) from the stress-free temperature and may partially relieve the compressive radial stresses and weaken the mechanical interlocking. In addition, the static frictional stresses at the fibre/matrix interface will decrease due to the reduction of the compressive radial stresses (since the frictional stresses are proportional to the radial stresses) and further reduce the interfacial shear strength (IFSS) [16,19]. The increase of temperature also diminished the ability of the matrix to transfer load to the fibres, by causing a significant drop in the elastic modulus of the matrix at temperatures above the T_g (as shown in Fig. 2). An effective stress transfer between the matrix and the fibres is vital for a high IFSS and is directly related to the matrix elastic modulus, as it has been previously demonstrated in literature [17,18,36,37].

All series showed a large drop in LSS at high temperatures, a drop that was in line with the evolution of the elastic modulus of PPS with temperature (Fig. 2); this phenomenon demonstrates the heavy dependence of LSS on the elastic modulus of the matrix. However, the elastic modulus of the matrix is not only influenced by the temperature but by the crystallinity degree of the matrix as well [14,15]. The latter varied substantially between the three series (Fig. 1) and, as shown in Fig. 2 and in Fig. 19, the temperature dependence of elastic modulus and LSS were also different among the three series. The next paragraphs attempt to connect the LSS of the three series to the crystallinity degree of PPS at the weldline.

The role of crystallinity on the weld performance appeared to be more critical at low and high temperatures (-50 °C, 90 °C and 120 °C).

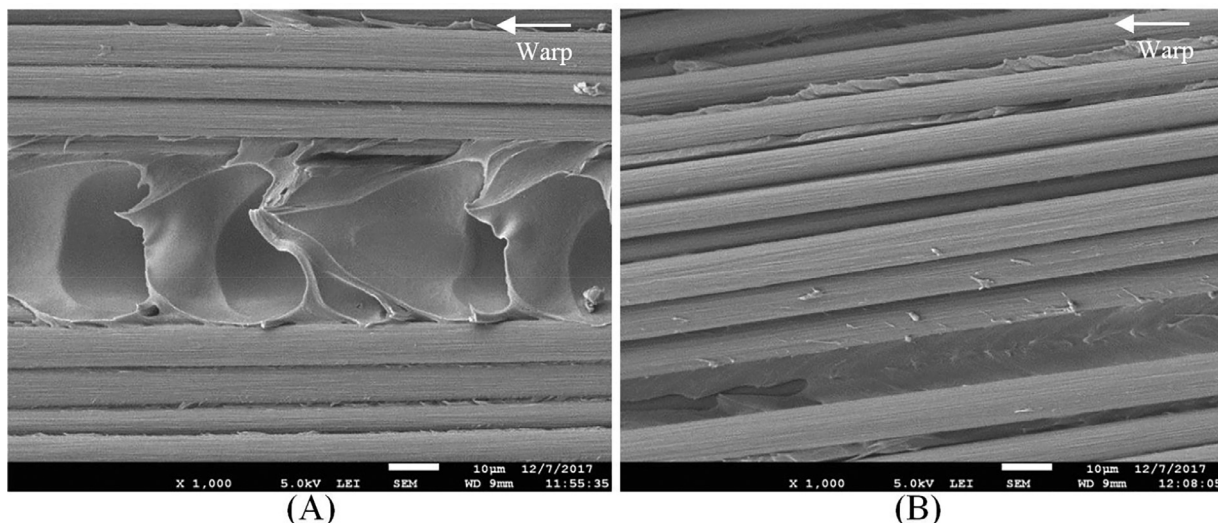


Fig. 18. SEM micrographs of locations A and B of Fig. 17: (A) & (B) Extensive fibre/matrix debonding accompanied by ductile failure.

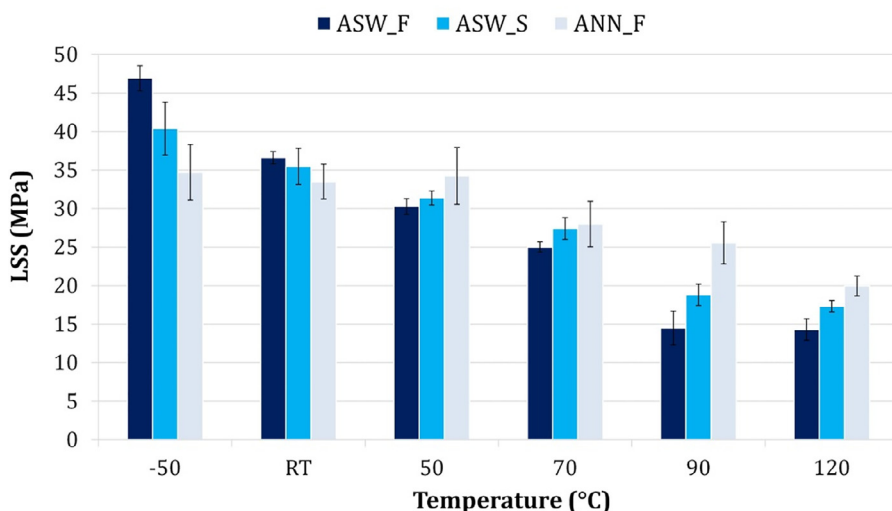


Fig. 19. Temperature dependence of lap shear strength of ASW_F, ASW_S, and ANN_F.

In Fig. 19 it can be seen that between RT and 70 °C there were small differences in LSS among the three series at each temperature, while at the extreme temperatures significant differences were observed. At -50 °C, the higher toughness and ductility of amorphous PPS [26] was probably favourable for the ASW_F specimens, thus, contributing to the higher LSS. The examination of the fracture surfaces revealed that at -50 °C the matrix failure was both ductile and brittle in all three series. However, ASW_F exhibited more areas of ductile failure at -50 °C than both ASW_S and ANN_F, which could be attributed to the amorphous state of PPS at the weldline of ASW_F specimens. It is noted though, that the occurrence of brittle fracture can also be promoted by a number of additional factors: (i) in the as-welded joints the failure progressed in the 2nd ply, where the cooling rate during welding could have been lower than it was in the weldline and, therefore, the degree of crystallinity would have been higher, leading to a stiffer and more brittle matrix; and (ii) the failure in a SLS test is sudden, thus, a more unstable crack occurred promoting brittle fracture [35,38,39], especially at low temperatures where the failure loads were high. The occurrence of 2nd ply failure in both ASW_F and ASW_S joints could also indicate a higher (interlaminar) peel strength of the former, considering the higher LSS of ASW_F. Taking into account the high cooling rates measured at the weldline of ASW_F [20] it could be argued that the matrix in the 2nd ply of ASW_F adherends was of lower crystallinity than that of ASW_S, resulting in higher peel strength. However, the X_C of PPS in the plies adjacent to the weldline of either ASW_F or ASW_S has not been measured; therefore, it remains unclear whether the peel strength inside the ASW_F adherends was higher than the peel strength inside the ASW_S adherends. Further investigation is required in order to characterise the crystallinity and the mechanical performance of the inner plies of the adherends.

Regarding the LSS of ANN_F at -50 °C it seems that it was also compromised by the presence of voids which most likely formed during annealing. The failure propagated easier through the voids, instead of occurring in the 1st and 2nd plies as in the as-welded joints, resulting in lower strength. In addition, the presence of voids was most likely the reason for the high scatter in the LSS of the ANN_F specimens at most temperatures, since the size and location of the voids were distributed across the overlap, leading to variations in strength. The cause of void formation is not clear to the authors, however, two possibilities are the shrinkage due to crystallization, and/or the absence of pressure during the annealing process. Further investigation is required to determine the origin of the voids, however, it goes beyond the scope of this study.

At high temperatures (90 °C and 120 °C) the presence of crystallinity appeared to be beneficial. The decrease in LSS at 90 °C with respect to RT was smaller for ANN_F, than the one for ASW_F (Fig. 19), a behaviour

that could be associated to the higher crystallinity of the former, as explained in what follows. As discussed previously, the significant drop in the elastic modulus of the matrix at temperatures higher than the T_g can deteriorate the stress transfer between the matrix and the fibres and eventually cause a reduction in LSS. As illustrated in Fig. 2, the T_g of annealed PPS is higher than the T_g of amorphous PPS. Thus, in the vicinity of 90 °C, the stress transfer between PPS and CF would be more efficient for ANN_F than ASW_F, resulting in a stronger fibre/matrix interfacial strength for the former and, essentially, in a higher LSS. However, the glass transition temperature is closely related to the crystallinity degree of the matrix: in Figs. 1 and 2 it can be seen that higher crystallinity degree is linked to a higher T_g. The shift of the glass transition to higher temperatures with increasing crystallinity has been observed by several researchers as well [27–29]. The mobility of the non-crystalline chain segments is hindered by the crystalline lamellae, especially in polymers with a semi-rigid backbone like PPS [28]. The effect of crystallinity on LSS is also demonstrated in the LSS of ASW_S at 90 °C (Fig. 19), which was in between the LSS of ASW_F and ANN_F. As shown in Fig. 1, the slower welding process resulted in PPS of moderate crystallinity degree, higher than that of ED_F and lower than that of ANN_Ref.

Another demonstration of the influence of crystallinity degree on the weld performance in relation with temperature, is the thermal expansion behaviour of PPS: the increase in the thermal expansion rate of annealed PPS took place around 92 °C due to the restrictions imposed by the crystalline domains on the chain mobility. On the contrary, the significant thermal expansion of amorphous PPS occurred at a lower temperature, around 83 °C, contributing to the reduction in LSS of ASW_F at 90 °C.

Furthermore, at 120 °C the negligible LSS reduction of ASW_F with respect to 90 °C occurred primarily due to the cold crystallization of PPS at 120 °C (during conditioning of the welded joints prior to mechanical testing). Fig. 1 shows a major increase in X_C due to conditioning of the welded joints at 120 °C for 10 minutes, Fig. 2 shows a sharp increase in the elastic modulus of PPS around 120 °C, and Fig. 3 illustrates a decrease in the thermal expansion rate of PPS right after the shrinkage corresponding to cold crystallization. On the basis of this evidence, and taking into consideration the earlier discussion on the mechanisms governing the IFSS, it can be argued that the increase in X_C of PPS due to cold crystallization acted as a competing mechanism against the negative effect of the further decrease in ΔT , by increasing the elastic modulus of PPS and the IFSS of CF/PPS. A similar behaviour was observed for the ASW_S specimens at 120 °C, which displayed a minor decrease in LSS of 8% with respect to 90 °C. The ASW_S specimens were cold-crystallized as well during conditioning prior to testing (Fig. 1), however, contrarily to the ASW_F specimens which changed from an amorphous state to a semi-crystalline state, the former already possessed a moderate crys-

tallinity, therefore, the increase in X_C was probably not as pivotal as it was for the LSS of ASW_F specimens. It is worth noting that despite the equal crystallinity degree of CON_F and CON_S (Fig. 1), the LSS of ASW_S at 120 °C was higher than the one of ASW_F. One would expect that the LSS of both series would be equal considering the equal X_C of CON_F and CON_S. However, as explained in section 3.1, the small size of the DSC samples (less than 10 mg) and the non-uniform crystallization might have caused a larger scatter in the DSC measurements of CON_F. This, perhaps, could have resulted in overestimating the X_C of CON_F. Another possibility is that, apart from the crystallinity degree, the crystal size and perfection might have also affected the weld performance. Considering that ED_S had already a moderate crystallinity degree while ED_F was nearly amorphous, it could be possible that despite the identical annealing conditions (10 min, 120 °C) and similar, if not equal, crystallinity degree, ASW_S obtained a different – and more favourable – crystalline structure than ASW_F. In addition, the larger scatter in the LSS between the two series (around 10% for ASW_F and 4% for ASW_S) also indicates larger variations in the weldline structure of ASW_F compared to the weldline structure of ASW_S. On the contrary, no changes in crystallinity were expected for ANN_F which was annealed at a high temperature and for a long duration (200 °C, 2 h); thus, 10 minutes of conditioning at 120 °C would not bring significant changes in the PPS state. Hence, as the T_g of annealed PPS occurred well below 120 °C (close to 100 °C, taken from the drop in storage modulus shown in Fig. 2), a sharp reduction in the LSS of ANN_F took place at 120 °C.

As it was previously mentioned, the higher toughness and ductility of amorphous PPS were proven to be beneficial for the LSS at –50 °C, however, their impact at high temperatures appears to be negligible. The effects of toughness and ductility at high temperatures have been studied by several researchers who reported that the G_{IC} propagation values increased with temperature due to increased matrix ductility [40–42]. However, since the failure in SLS tests is sudden, since the joint is mainly loaded in shear in the middle of the overlap [43], and considering the high peel stresses at the overlap edges of SLS joints [11], the G_{IC} initiation values are considered to be more relevant for the SLS tests than the G_{IC} propagation values. With respect to the former, Kim and Ye [40] found that at high temperatures the initiation values decreased, a phenomenon that they attributed to the weakened IFSS. Therefore, it is suggested that the beneficial effect of higher matrix ductility on the Mode-I interlaminar fracture toughness at high temperatures was negated by the poor IFSS.

Finally, taking into account the discussion on the benefits of amorphous PPS state and semi-crystalline PPS state at the weldline, it is suggested that between RT and 70 °C the higher toughness and ductility of amorphous PPS counterbalanced the higher stiffness and higher IFSS of semi-crystalline PPS, resulting in minor differences in LSS among the three series.

6. Conclusions

This study elucidated the effect of temperature on the lap shear strength and the failure mechanisms of ultrasonically welded CF/PPS joints by linking the weld performance to the degree of crystallinity of PPS at the weldline. Single-lap shear tests were performed at temperatures ranging from –50 °C to 120 °C on two series of welded joints (as-welded), one with amorphous and one with semi-crystalline weldline, and on one series of annealed welded joints.

The single-lap shear tests showed an overall trend of decreasing lap shear strength with increasing temperature, with the exception of two temperature regions: –50 °C to 50 °C for the annealed series, and 90 °C to 120 °C for the two as-welded series, where the LSS remained virtually constant. It was suggested that the primary failure mechanism of the two as-welded series at all temperatures, except –50 °C where matrix fracture occurred, was fibre/matrix debonding, a failure mode that became more prevalent with increasing temperature, especially at and above

the glass transition temperature of PPS. The annealed series exhibited cohesive failure in all specimens at all temperatures but its occurrence diminished with increasing temperature, while fibre/matrix debonding became more pronounced. It was also found that the annealed specimens exhibited porosity in the weldline, which was related to the annealing process, and played a primary role in causing cohesive failure.

Higher degree of crystallinity of PPS at the weldline was found to be beneficial at high temperatures (90 °C and 120 °C) probably due to the higher elastic modulus and, hence, to the higher fibre/matrix interfacial strength compared to amorphous PPS. Cold crystallization of both as-welded series due to conditioning at 120 °C prior to mechanical testing was found to have a profound effect on the LSS, causing the LSS of both series to remain virtually constant at 90 °C and 120 °C. However, at low temperatures (–50 °C) amorphous weldline was proven to be more beneficial, most likely due to the higher toughness and ductility of amorphous PPS compared to semi-crystalline PPS. Furthermore, between room temperature and 70 °C only minor differences in LSS were observed amongst all series, indicating that there was little effect of the degree of crystallinity above room temperature to just below the glass transition temperature.

In conclusion, this study has demonstrated that both states of PPS – amorphous and semi-crystalline – can be beneficial for the performance of ultrasonically welded CF/PPS joints in dry conditions, depending on the service temperature. Arguably, a semi-crystalline PPS would allow joints to be used at higher temperatures while an amorphous PPS, as long as the service temperature remained below the glass transition temperature, could be preferable due to its even better performance at low temperatures. Please note that these conclusions refer exclusively to welded joints in dry conditions and not exposed to moisture or any chemical environments. Hence, further studies on the chemical resistance of ultrasonically welded CF/PPS joints are required to identify the material limits.

Declaration of Competing Interest

The authors confirm that there are no known conflicts of interest associated with this publication and there has been no significant financial support for this work that could have influenced its outcome.

Acknowledgements

This study is part of the Thermoplastic Affordable Primary Aircraft Structure 2 (TAPAS2) project, financed by Netherlands Enterprise Agency of the Ministry of Economic Affairs.

References

- [1] N Koutras, IF Villegas, R. Benedictus, Influence of temperature on the strength of resistance welded glass fibre reinforced PPS joints, *Compos.: Part A* 105 (2018) 57–67.
- [2] V Rohart, M Dubé, L Laberge Lebel, Effects of temperature on the apparent lap shear strength of resistance-welded carbon fibre/thermoplastic composite joints, in: *Proceedings of the International SAMPE Technical Conference*, 2018, pp. 1–10.
- [3] MN Tolunay, PR Dawson, KK. Wang, Heating and bonding mechanisms in ultrasonic welding of thermoplastics, *Polym. Eng. Sci.* 23 (13) (1983) 726–733.
- [4] A Benatar, TG. Gutowski, Ultrasonic welding of PEEK graphite APC-2 composites, *Polym. Eng. Sci.* 29 (23) (1989) 1705–1721.
- [5] H. Potente, Ultrasonic welding – principles and theory, *Mater. Des.* 5 (5) (1984) 228–234.
- [6] A Levy, S Le Corre, IF Villegas, Modeling of the heating phenomena in ultrasonic welding of thermoplastic composites with flat energy directors, *J. Mater. Process. Technol.* 214 (2014) 1361–1371.
- [7] IF. Villegas, Strength development versus process data in ultrasonic welding of thermoplastic composites with flat energy directors and its application to the definition of optimum processing parameters, *Compos.: Part A* 65 (2014) 27–37.
- [8] IF. Villegas, In situ monitoring of ultrasonic welding of thermoplastic composites through power and displacement data, *J. Thermoplast. Compos. Mater.* 28 (2015) 66–85.
- [9] G Palardy, IF. Villegas, On the effect of flat energy directors thickness on heat generation during ultrasonic welding of thermoplastic composites, *Compos. Interfaces* 24 (2) (2017) 203–214.
- [10] IF Villegas, G. Palardy, Ultrasonic welding of CF/PPS composites with integrated triangular energy directors: melting, flow and weld strength development, *Compos. Interfaces* 24 (5) (2017) 515–528.

- [11] T Zhao, G Palardy, IF Villegas, C Rans, M Martinez, R. Benedictus, Mechanical behaviour of thermoplastic composites spot-welded and mechanically fastened joints: a preliminary comparison, *Compos. Part B: Eng.* 112 (2017) 224–234.
- [12] B Jongbloed, J Teuwen, G Palardy, IF Villegas, R. Benedictus, Continuous ultrasonic elding of thermoplastic composites: enhancing the weld uniformity by changing the energy director, *J. Compos. Mater.* 0 (0) (2019) 1–13.
- [13] B Jongbloed, J Teuwen, R Benedictus, IF. Villegas, On differences and similarities between static and continuous ultrasonic welding of thermoplastic composites, *Compos. Part B* 203 (2020) 108466.
- [14] MF Talbott, GS Springer, LA. Berglund, The effects of crystallinity on the mechanical properties of PEEK polymer and graphite fiber reinforced PEEK, *J. Compos. Mater.* 21 (1987) 1056–1081.
- [15] Spruiell JE, Janke CJ. A review on the measurement and development of crystallinity and its relation to properties in neat poly(phenylene sulfide) and its fiber reinforced composites. Technical Report, Oak Ridge National Laboratory, 2004.
- [16] JL Thomason, L. Yang, Temperature dependence of the interfacial shear strength in glass-fibre polypropylene composites, *Compos. Sci. Technol.* 71 (2011) 1600–1605.
- [17] V Rao, LT. Drzal, The temperature dependence of interfacial shear strength for various polymeric matrices reinforced with carbon fibers, *J. Adhes.* 37 (1992) 88–95.
- [18] V Rao, LT. Drzal, The dependence of interfacial shear strength on matrix and interphase properties, *Polym. Compos.* 12 (1) (1991) 48–56.
- [19] L Di Landro, M. Pegoraro, Evaluation of residual stresses and adhesion in polymer composites, *Compos. Part A* 27A (1996) 847–853.
- [20] N Koutras, J Amirdine, N Boyard, IF Villegas, R. Benedictus, Characterisation of crystallinity at the interface of ultrasonically welded carbon fibre PPS joints, *Compos. Part A* 125 (2019) 105574.
- [21] SL Gao, JK. Kim, Cooling rate influences in carbon fibre/PEEK composites. Part 1. Crystallinity and interface adhesion, *Compos.: Part A* 31 (2000) 517–530.
- [22] SL Gao, JK. Kim, Correlation among crystalline morphology of PEEK, interface bond strength, and in-plane mechanical properties of Carbon/PEEK composites, *J. Appl. Polym. Sci.* 84 (2002) 1155–1167.
- [23] E Schulz, G Kalinka, W. Auersch, Effect of transcrystallization in carbon fiber reinforced poly(p-phenylene sulfide) composites on the interfacial shear strength investigated with the single fiber pull-out test, *J. Macromol. Sci. Part B* 35 (3-4) (1996) 527–546.
- [24] B Liu, X Wang, S Long, J. Yang, Interfacial micromechanics of carbon fiber-reinforced polyphenylene sulfide composites, *Compos. Interfaces* 21 (4) (2014) 359–369.
- [25] SL Gao, JK. Kim, Cooling rate influences in carbon fibre/PEEK composites. Part II: interlaminar fracture toughness, *Compos.: Part A* 32 (2001) 763–774.
- [26] F Sacchetti, WJB Groupe, LL Warnet, IF. Villegas, Effect of cooling rate on the interlaminar fracture toughness of unidirectional carbon/PPS laminates, *Eng. Fract. Mech.* 203 (2018) 126–136.
- [27] RC Zhang, R Li, A Lu, Z Jin, B Liu, Z. Xu, The glass transition temperature of poly(phenylene sulfide) with various crystallinities, *Polym. Int.* 62 (2013) 449–453.
- [28] RK Krishnaswamy, JF Geibel, BJ. Lewis, Influence of semicrystalline morphology on the physical aging characteristics of poly(phenylene sulfide), *Macromolecules* 36 (2003) 2907–2914.
- [29] A Jonas, R. Legras, Relation between PEEK semicrystalline morphology and its sub-glass relaxations and glass transition, *Macromolecules* 26 (1993) 813–824.
- [30] ASTM Standard D 3518/D 3518M – 94Standard Test Method for In-Plane Shear Response of Polymer Composite Materials by Tensile Test of a $\pm 45^\circ$ Laminate, ASTM International, West Conshohocken, PA, 2001.
- [31] P. Huo, P. Cebe, Effects of thermal history on the rigid amorphous phase in poly(phenylene sulfide), *Colloid Polym. Sci.* 270 (1992) 840–852.
- [32] A Maffezzoli, JM Kenny, L. Nicolais, Thermal analysis of thermoplastic matrices for advanced composite materials: poly(phenylene sulphide), *Thermochim. Acta* 199 (1992) 133–146.
- [33] JA Barnes, GE. Byerly, The formation of residual stresses in laminated thermoplastic composites, *Compos. Sci. Technol.* 51 (1994) 479–494.
- [34] KP. Menard, *Dynamic Mechanical Analysis. A Practical Introduction*, 3rd edition, CRC Press, 2008.
- [35] D Purslow, Matrix fractography of fibre-reinforced thermoplastics, Part 1. Peel failures, *Composites* 18 (5) (1987) 365–374.
- [36] Q Zhang, S Liang, G Sui, X. Yang, Influence of matrix modulus on the mechanical and interfacial properties of carbon fiber filament wound composites, *RSC Adv.* 5 (2015) 25208–25214.
- [37] NR Sottos, L Li, G. Agrawal, The effects of interphase properties on interfacial shear strength in polymer matrix composites, *J. Adhes.* 45 (1994) 105–124.
- [38] D Purslow, Matrix fractography of fibre-reinforced thermoplastics. Part 2. Shear failures, *Composites* 19 (2) (1988) 115–126.
- [39] E. Greenhalgh, *Failure Analysis and Fractography of Polymer Composites*, CRC Press, 2009.
- [40] K.Y. Kim, L. Ye, K.M. Phoa, Interlaminar fracture toughness of CF/PEI and GF/PEI composites at elevated temperatures, *Appl. Compos. Mater.* 11 (2004) 173–190.
- [41] K.D. Cowley, P.W.R. Beaumont, The interlaminar and intralaminar fracture toughness of carbon-fibre/polymer composites: The effect of temperature, *Compos. Sci. Technol.* 57 (1997) 1433–1444.
- [42] S. Hashemi, A.J. Kinloch, J.G. Williams, The effects of geometry, rate and temperature on the Mode I, Mode II and Mixed-Mode I/II interlaminar fracture of carbon-fibre/poly(ether-ether ketone) composites, *J. Compos. Mater.* 24 (9) (1990) 918–956.
- [43] LFM da Silva, A. Öchsner, *Modeling of Adhesively Bonded Joints*, Springer, Heidelberg, 2008.